

RARE EVENT MODELING WITH SELF-REGULARIZED NORMALIZING FLOWS: WHAT CAN WE LEARN FROM A SINGLE FAILURE?

Anonymous authors

Paper under double-blind review

ABSTRACT

Increased deployment of autonomous systems in fields like transportation and robotics has led to a corresponding increase in safety-critical failures. These failures are difficult to model and debug due to the relative lack of data: while normal operations provide tens of thousands of examples, we may have only seconds of data leading up to the failure. This scarcity makes it challenging to train generative models of rare failure events, as existing methods risk either overfitting to noise in the limited failure dataset or underfitting due to an overly strong prior. We address this challenge with CALNF, or calibrated normalizing flows, a self-regularized framework for posterior learning from limited data. CALNF achieves state-of-the-art performance on data-limited failure modeling problems and enables a first-of-a-kind case study of the 2022 Southwest Airlines scheduling crisis.

1 INTRODUCTION

When complex systems fail, the first step towards recovery is understanding the factors that lead to failure. Modeling failures and other rare events is challenging because the limited amount of available data. While much work has been done on preemptive failure prediction in simulation (Corso et al., 2022; O’ Kelly et al., 2018; Sinha et al., 2020; Dawson & Fan, 2023; Delecki et al., 2023; Zhong et al., 2023), and online failure detection (Keipour et al., 2021; Hendrycks et al., 2018; Gudovskiy et al., 2022; Kang et al., 2022; Najari et al., 2022; Garg et al., 2023), relatively little work has been done on post-event failure modeling from observational data.

In failure modeling problems, we seek to infer the hidden factors contributing to an observed failure by learning a posterior distribution over those factors. When observational data are plentiful, deep generative models can be powerful tools for solving these problems, but these methods struggle when only a few examples are available. To solve rare event modeling problems that arise in domains like robotics and networked cyberphysical systems, we need new ways of training generative models in data-constrained settings.

Formally, we frame rare event modeling as a *data-constrained Bayesian inverse problem* where we aim to infer the distribution of latent variables z from noisy observations x of a stochastic process $x \sim p_\theta(x|z; y)$, where θ are unknown process parameters and y are known context variables, **all real-valued** (Stuart, 2010). Given nominal observations $\mathcal{D}_0 = \{x_0^{(i)}, y_0^{(i)}\}_{i=1}^{N_0}$ and a much smaller set of target observations $\mathcal{D}_t = \{x_t^{(i)}, y_t^{(i)}\}_{i=1}^{N_t}$, where $N_t \ll N_0$, we aim to learn an approximation of the posterior distribution

$$q_\phi(z) \approx p_\theta \left(z \mid \{x_t^{(i)}, y_t^{(i)}\}_{i=1}^{N_t} \right). \quad (1)$$

Note that this problem is distinct from the rare event simulation problem considered in O’ Kelly et al. (2018); Sinha et al. (2020); Gao et al. (2023), and Dawson & Fan (2023). While we focus on learning the distribution of failures from small, fixed number of real-world data points, these methods assume the ability to sample and label an arbitrary number of new failure examples in simulation.

In data-constrained settings, a common approach to solving inverse and few-shot generative modeling problems is to use the nominal observations to train a deep model of the prior distribution, then use this prior to regularize q_ϕ (e.g. by penalizing the divergence between q_ϕ and the learned prior,

Asim et al. (2020); Liu et al. (2023); Abdollahzadeh et al. (2023); Zhang et al. (2019); Ojha et al. (2021); Higgins et al. (2016)). Unfortunately, it can be difficult to specify the appropriate amount of regularization *a priori*, particularly when the distribution of z differs between the nominal and target datasets (as is often the case in failure modeling problems).

In this paper, we address this challenge by developing CALNF, or calibrated normalizing flows. To make full use of available data, CALNF amortizes inference over both the nominal and target datasets, learning a shared representation for both posteriors. To prevent overfitting, CALNF first learns a low-dimensional embedding for a family of candidate posteriors then searches over this low-dimensional space to find an optimal representation of the target posterior. Our method achieves state-of-the-art performance on a range of data-constrained inference benchmarks, including several with real-world data from autonomous systems. We apply our method to a post-mortem analysis of the 2022 Southwest Airlines scheduling crisis, which stranded more than 2 million passengers and led to more than \$750 million in financial losses (Rose, 2023); our first-of-a-kind analysis suggests a mechanism by which failure propagated through the Southwest network.

2 BACKGROUND

Because the posterior in Eq. (1) is typically intractable to evaluate exactly, inverse problems are typically solved approximately, often using variational inference (Stuart, 2010). These methods approximate the true posterior by maximizing the evidence lower bound (ELBO, Kingma & Welling (2013)), often using deep non-parametric representations like normalizing flows for q_ϕ (Tabak & Vanden-Eijnden, 2010; Rezende & Mohamed, 2015).

$$\mathcal{L}(\phi, \theta, \mathcal{D}) = \mathbb{E}_{(x,y) \in \mathcal{D}} \mathbb{E}_{z \sim q_\phi(z)} [\log p_\theta(x, z; y) - \log q_\phi(z)]. \quad (2)$$

A particular challenge in data-constrained settings is that deep models tend to overfit the particular target samples used for training, as shown in Fig. 1c. As the following result illustrates, the representational power of these models makes them highly sensitive when trained on small datasets.

Lemma 1. *Let $\mathcal{D} = \{z^{(i)}\}_{i=1}^N$ be sparse dataset with distance $O((LN)^{-1/(d+1)})$ between points (the precise limit is given in the appendix), and let $q_\phi(z)$ be a model capable of representing any L -Lipschitz probability density. If $\phi(\mathcal{D})$ are the parameters of the maximum likelihood estimator¹ given \mathcal{D} , then the optimal solutions trained on datasets differing by one point $\mathcal{D}_1 = \mathcal{D} \cup \{z^{(1)}\}$ and $\mathcal{D}_2 = \mathcal{D} \cup \{z^{(2)}\}$ will differ by Wasserstein distance $W_2(q_{\phi(\mathcal{D}_1)}, q_{\phi(\mathcal{D}_2)}) = \|z^{(1)} - z^{(2)}\|/N$.*

The proof relies on the fact that the optimal L -Lipschitz maximum likelihood estimator is $q_{\phi(\mathcal{D})}(z) = \sum_{z^{(i)} \in \mathcal{D}} \hat{\delta}(z - z^{(i)})$, where $\hat{\delta}(z) = \max(0, a - L\|z\|)$ is an L -Lipschitz approximation of $\delta(z)/N$ and a is a constant given in the appendix. Lemma 1 implies that small changes in the training data can lead to large changes in the learned distribution; as N becomes small, this sensitivity increases.

Two common strategies for reducing this sensitivity in non-sparse settings are *bootstrapping* (Efron, 1992), which trains an ensemble of models on random subsamples of the target data, and *prior*

¹We provide these results for maximum likelihood estimation, but similar results can be shown for maximum *a posteriori* or maximum ELBO contexts.

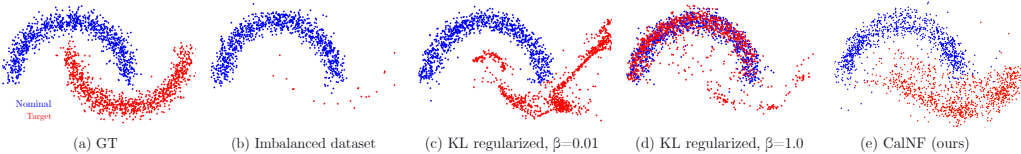


Figure 1: **Inference in data-constrained environments.** (a) The ground truth distribution. (b) An imbalanced dataset. (c) When the regularization strength β is too small, deep models overfit to noise in the target dataset. (d) When β is too large, the learned distribution underfits and struggles to distinguish between nominal and target distributions. (e) Our method learns a more accurate reconstruction of the target distribution using hyperparameter-insensitive self-regularization.

regularization (Asim et al., 2020), which uses a model trained on nominal data to regularize the target posterior. Unfortunately, both of these methods are difficult to apply to data-constrained problems.

Bootstrapping, or ensemble, methods are theoretically well-motivated (Efron, 1992; Breiman, 1996) but do not fully avoid data sensitivity issues when applied to deep models (Nixon et al., 2020). In fact, it can be shown that bootstrapping has no effect on data sensitivity in highly data-constrained environments.

Lemma 2. Consider the setting from Lemma 1. Let \mathcal{D}_i be K subsampled datasets created by sampling N points with replacement from the original \mathcal{D} . Let $\phi(\mathcal{D}_i)$ be parameters of the maximum likelihood estimator for each \mathcal{D}_i and define the ensemble model $q_{\text{ensemble}}(z) = \sum_{i=1}^K q_{\phi_i}(z)/K$. As $K \rightarrow \infty$, the ensemble model recovers the solution of the non-bootstrapped problem; i.e. $q_{\text{ensemble}}(z) \rightarrow q_{\phi(\mathcal{D})}(z)$.

The second strategy, prior regularization, is common in the few-shot learning literature, particularly for image generation tasks (Asim et al., 2020; Higgins et al., 2016; Abdollahzadeh et al., 2023). These methods use a large dataset to learn the nominal posterior distribution, then use that nominal posterior to regularize the target posterior:

$$\phi_0 = \operatorname{argmax}_{\phi} \mathcal{L}(\phi, \theta, \mathcal{D}_0) \quad \phi_t = \operatorname{argmax}_{\phi} \mathcal{L}(\phi, \theta, \mathcal{D}_t) - \beta D_{KL}(q_{\phi_0}, q_{\phi}) \quad (3)$$

This penalty allows the large number of nominal samples to regularize the distribution learned from the target data, but there are two issues with this approach. First, it is difficult to choose an appropriate penalty strength β *a priori*, as illustrated using the toy example in Fig. 1. If β is too small, the model will overfit to the target data (Fig. 1c), but if β is too large then the model will underfit the target in favor of learning the nominal distribution (Fig. 1d). Moreover, even if we were able to select an optimal β , many practical failure modeling problems involve a large shift between the nominal and target distributions, [in which case regularizing between these distributions may not be appropriate](#).

In order to effectively train deep generative models of rare failure events, we will need to address two key questions. First, building upon prior regularization: can we adapt the amount of regularization based on the available data rather than specifying a regularization penalty *a priori*? Second, building upon bootstrapping: can we share information between model components to learn robustly in data-constrained contexts?

2.1 RELATED WORK

A number of recent works have explored various forms of prior regularization, mostly in the context of image generation tasks (see Abdollahzadeh et al. (2023) for a survey). Asim et al. (2020) use a deep prior model trained on large image datasets to regularize single-shot maximum likelihood estimation for image denoising. Liu et al. (2023) combine prior regularization with graduated optimization for image reconstruction, gradually increasing the regularization strength over multiple inference rounds. Ojha et al. (2021) pre-train a model on a large open image dataset, then fine-tune to smaller image datasets with a loss function that preserves relative difference and similarity across domains. Kong et al. (2022) focus on generative adversarial networks (GANs) and regularize the generator’s latent space by sampling points in between sparse target data. Other works rely on data augmentation, either using hand-designed heuristics Wang et al. (2020), which must be re-derived for each new problem domain, or pre-trained generative models Tran et al. (2017); Zheng et al. (2023), which require a minimum amount of data from similar examples.

3 METHOD: CALIBRATED NORMALIZING FLOWS

To address the challenges from Section 2, we propose a novel framework for rare event modeling: calibrated normalizing flows, or CALNF. This method involves two steps, illustrated in Fig. 2. First, we learn a low-dimensional embedding for a family of probability distributions that includes both the nominal posterior and several candidate target posteriors. We then search over this low-dimensional space to find the optimal representation of the target posterior. To ensure that the embedding space is well behaved, we apply regularization between candidate target posteriors. This self-regularization, combined with implicit regularization from our use of a single, shared representation for both the target and nominal posteriors, allows CALNF to efficiently learn the posterior without overfitting.

The first step in our framework is to learn an embedding for a family of candidate probability distributions. To do this, we randomly sample K subsets of the target data $\mathcal{D}_t^{(1)}, \dots, \mathcal{D}_t^{(K)}$, then train

a single conditional normalizing flow $q_\phi(z; c)$ to learn a mapping from a low-dimensional label c to the posterior distribution conditioned on each of these subsets. We identify the posterior for each target subset using one-hot labels $\mathbf{1}_i$ and use the zero label $\mathbf{0}_K$ to identify the nominal posterior; i.e.:

$$q_\phi(z; \mathbf{0}_K) \approx p(z|\mathcal{D}_0), \quad q_\phi(z; \mathbf{1}_i) \approx p(z|\mathcal{D}_t^{(i)}), \quad i = 1, \dots, K$$

Once posteriors have been learned for each of these subsets, we calibrate the model by holding the model weights ϕ constant and searching for an optimal label c^* such that $q_\phi(z; c^*) \approx p(z|\mathcal{D}_t)$.

This training process is shown in more detail in Algorithm 1. This algorithm modifies the standard variational inference training process in two ways: by training on multiple random subsets of the target data, and by interleaving model updates and label calibration. To begin, we split the target training data into K random subsets with one-hot labels and train the model to learn the posterior for each subset. Each subset \mathcal{D}_t^i is created by independently drawing N_t samples from \mathcal{D}_t with replacement. We denote the empirical ELBO given dataset \mathcal{D} as

$$\mathcal{L}(\phi, c, \mathcal{D}) = \frac{1}{|\mathcal{D}|} \sum_{(x,y) \in \mathcal{D}} \mathbb{E}_{z \sim q_\phi(z;c)} [\log p(x, z; y) - \log q_\phi(z; c)]. \quad (4)$$

The model is trained with three objectives: to maximize the ELBO on each target subset (with one-hot labels), the nominal data (with a zero label), and the full target dataset (using the calibrated label c^*). In addition, to improve the conditioning of the embedding space, we add a regularization term on the divergence between the posterior distributions learned for each target subset, yielding the loss:

$$L(\phi, c) = -\frac{1}{K} \sum_{i=1}^K \mathcal{L}(\phi, \mathbf{1}_i, \mathcal{D}_t^{(i)}) - \mathcal{L}(\phi, \mathbf{0}_K, \mathcal{D}_0) - \mathcal{L}(\phi, c, \mathcal{D}_t) + \beta \sum_{i \neq j} D_{KL}(q_\phi(\cdot; \mathbf{1}_i), q_\phi(\cdot; \mathbf{1}_j)) \quad (5)$$

This additional regularization term reflects the fact that the target subsamples $\mathcal{D}_t^{(i)}$ are identically distributed, so the divergence between the candidate posteriors learned for each subsample should be small, and we show empirically that CALNF performs well for a range of β . The mixture label c^* is initialized at $[1/K, \dots, 1/K]$ and updated to maximize $c^* = \arg \max_c \mathcal{L}(\phi, c, \mathcal{D}_t)$. In practice, this is equivalent to jointly optimizing $(\phi, c^*) = \arg \min L(\phi, c^*)$, but we show these optimization steps separately in Alg. 1 to emphasize the different objectives.

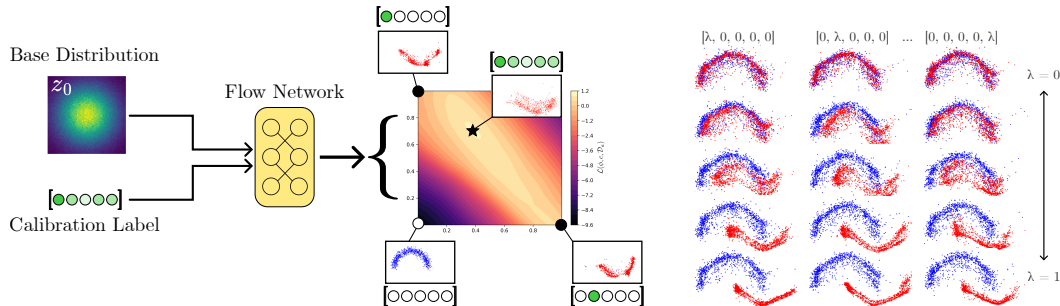


Figure 2: **(Left) CalNF architecture:** A normalizing flow is trained on random subsamples of the target data and the full nominal dataset, using one-hot labels to identify different subsamples (\bullet) and the zero vector to identify the nominal data (\circ). The model is calibrated by freezing the model parameters and optimizing the label on the entire target dataset (\star). **(Right) Target candidates:** The nominal posterior $q_\phi(z; \mathbf{0})$ (blue) and the family of candidate distributions for the target posterior $q_\phi(z; \lambda \mathbf{1}_i)$, shown for varying values of the calibration label.

Algorithm 1 Calibrated Normalizing Flows

Input: Nominal data \mathcal{D}_0 , target data \mathcal{D}_t , step size γ , number of target subsamples K , self-regularization β
Output: Model parameters ϕ and calibrated label c^*
for $k = 1, \dots, K$ **do**
 $\mathcal{D}_t^{(k)} \leftarrow N$ -element random subsample of \mathcal{D}_t
end for
Initialize ϕ, c^*
while ϕ not converged **do**
Update model $\phi \leftarrow \phi - \gamma \nabla_{\phi} L(\phi, c^*)$
Update calibration $c^* \leftarrow c^* - \gamma \nabla_c L_{\text{cal}}(\phi, c^*)$
end while

3.1 THEORETICAL ANALYSIS

The secondary optimization of c^* is one of the main differences between CALNF and traditional bootstrapped ensembles (which combine the target candidates in a mixture model rather than optimizing in a lower-dimensional label space). In this section, we provide theoretical motivation for this decision, showing that learning a mapping from labels c to candidate distributions *implicitly* regularizes the learned target posterior.

In particular, consider the Wasserstein metric $W_2(p_1, p_2) = \inf_{\gamma} [\mathbb{E}_{z_1, z_2 \sim \gamma} \|z_1 - z_2\|^2]^{1/2}$ where γ is a coupling of probability distributions p_1 and p_2 . The result shows that CALNF, in addition to explicitly regularizing the divergence between target candidates, also provides implicit regularization of the W_2 metric between the learned nominal and calibrated target posteriors.

Theorem 1. *If the flow map $f_{\phi}(z, c)$ is L -Lipschitz in the second argument, then the Wasserstein distance between the nominal and target posteriors is bounded; $W_2(q_{\phi}(z, \mathbf{0}_K), q_{\phi}(z, c^*)) \leq L \|c^*\|$*

A proof is included in the appendix, along with L for common normalizing flow architectures.

4 EXPERIMENTS

4.1 BENCHMARK PROBLEMS

This section describes the benchmark problems used in our experiments; the first is newly developed for our study, but the rest are previously-published benchmarks (Keipour et al., 2021; Deng et al., 2022). We also include the toy 2D problem in Fig. 1 ($N_0 = 10^3, N_t = 20$). More details are provided in the appendix, and we will provide open-source code and data for each upon publication.

Air traffic disruptions We develop a stochastic queuing model of the Southwest Airlines network using publicly available arrival and departure data, based on (Pyrgiotis et al., 2013). The latent variables represent travel times, runway delays, and overnight aircraft reserves. The context includes flight schedules, and observations include actual departure and arrival times. Nominal and failure data from between Dec. 1 through Dec. 20 and Dec. 21 through Dec. 30, respectively, are used for the four busiest airports. The four-airport sub-network has 24 latent variables. We train using $N_0 = 9$ and $N_t = 4$ and evaluate on 4 held-out failure data points (each data point is a single day with between 88–102 flights).

Aerial vehicle control We consider a failure detection benchmark for unmanned aerial vehicles (UAVs) using the ALFA dataset (Keipour et al., 2021). This dataset includes real-world data from a UAV during normal flight and during failures with various deactivated control surfaces. The latent variable z parameterizes the nonlinear attitude dynamics and has 21 dimensions, y includes the current and commanded states, and x is the next state. We train on 10 nominal trajectories ($N_0 = 2235$) and 1 failure trajectory ($N_t = 58$) and evaluate on a held-out failure trajectory (69 points).

Geophysical imaging Seismic waveform inversion (SWI) is a well-known geophysics problem used as a benchmark for inference and physics-informed learning (Gouveia & Scales, 1998; Deng

Table 1: ELBO (nats/dim) on held-out anomaly data on benchmark problems. 2D and SWI use unseen synthetic data for the test set; all other cases withhold half of the target data for testing. Mean and standard deviation across four seeds are reported. \dagger scaled by $\times 10^{-3}$

	2D	SWI	UAV	ATC
	nats/dim \uparrow	nats/dim † \uparrow	nats/dim \uparrow	nats/dim † \uparrow
KL-regularized ($\beta = 0.01$)	-3.22 \pm 0.13	44.7 \pm 0.58	2.87 \pm 1.42	-2.26 \pm 0.10
KL-regularized ($\beta = 0.1$)	-2.03 \pm 0.04	44.7 \pm 0.39	3.26 \pm 1.54	-2.23 \pm 0.09
KL-regularized ($\beta = 1.0$)	-1.04 \pm 0.06	44.3 \pm 0.40	3.02 \pm 1.19	-2.23 \pm 0.10
W_2 -regularized ($\beta = 0.01$)	-4.58 \pm 0.18	36.7 \pm 3.03	-1.75 \pm 4.53	-5.90 \pm 2.54
W_2 -regularized ($\beta = 0.1$)	-2.95 \pm 0.14	36.7 \pm 3.02	-1.54 \pm 4.31	-5.80 \pm 2.45
W_2 -regularized ($\beta = 1.0$)	-1.67 \pm 0.05	36.7 \pm 2.94	-2.13 \pm 5.79	-6.57 \pm 4.09
Ensemble	-0.84 \pm 0.14	46.1 \pm 0.42	6.65 \pm 0.98	-2.23 \pm 0.06
CALNF (ours)	-0.90 \pm 0.10	46.4 \pm 0.26	7.55 \pm 0.60	-2.11 \pm 0.13

et al., 2022; Zhang et al., 2016). SWI seeks to infer the properties of the Earth’s subsurface using seismic measurements, which are simulated using the elastic wave equation. This model uses latent variables z for subsurface density, context y for the source signal, and observations x for the seismic measurements (Richardson, 2023). The latent space has 100 dimensions (a 10×10 grid). We train on $N_0 = 100$ and $N_t = 4$ and evaluate on 500 synthetic samples.

4.2 BASELINES AND METRICS

Our main claim is that our CALNF framework is an effective way to learn the posterior when a small number of target data points are available. The most relevant comparisons are to the prior regularization and bootstrapping ensemble methods discussed in Section 2. In particular, we compare against three baselines from previously-published literature: prior regularization using KL divergence (based on Asim et al. (2020)), prior regularization using Wasserstein divergence (based on Finlay et al. (2020) and Onken et al. (2021)), and an ensemble method based on a mixture of normalizing flows (adapted from the generative ensembles proposed in Choi et al. (2019)). The two prior regularization baselines are sensitive to the hyperparameter β , so we report results for a range $\beta \in [0.01, 1.0]$. CALNF uses $K = 5$ and $\beta = 1.0$ for all problems, and Figs. 11 and 12 in the appendix shows the sensitivity of our method to varying K and β . We use $K = 5$ components for the ensemble baseline.

Since the large amount of nominal data makes it easy to fit the nominal distribution, we compare primarily on the basis of the evidence lower bound \mathcal{L} computed on held-out target data, reporting the mean and standard deviation over four random seeds. When useful, we also provide visual comparisons of the posterior distributions learned using different methods.

4.3 RESULTS & DISCUSSION

Our main empirical results are shown in Table 1. Our method achieves better performance on held-out target data than baselines on all problems. Of course, CALNF’s improved performance comes at the cost of increased training time, requiring K additional likelihood evaluations per step relative to the KL- and W_2 -regularized methods (and the same number of evaluations as the ensemble method). To qualitatively understand the difference in performance between these methods, Fig. 3 compares the learned target posteriors on the SWI problem (which lends itself to easy visualization) with the ground truth in 3a. We see that the KL- and W_2 -regularized and ensemble methods (Fig. 3b-d) do not infer the correct density profile from the target data, while only our method (Fig. 3e) is able to infer the correct shape. Fig. 4 shows CALNF’s prediction in the UAV problem on a held-out failure trajectory after training on only one other failure trajectory (and 10 nominal trajectories). These results suggests that our method is able to appropriately balance the information gained from the nominal distribution with the limited number of target data points.

We also provide the results of an ablation study in Table 8 in the supplementary material, comparing the ELBO achieved when we omit the calibration step (using a constant c), omit the nominal data, and remove the subsampling step. These results indicate that most of the performance improvement from CALNF is due to training on random subsamples of the target data. We observe that in cases

324
325
326
327
328
329
330
331
332
333
334
335

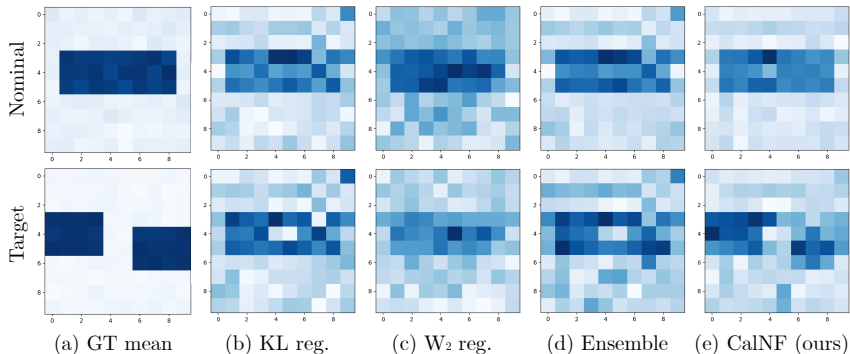


Figure 3: **Seismic waveform inversion.** (a) The ground truth nominal and target density profiles. (b-d) The posteriors fit using KL and W_2 regularization and CALNF (ours is the only method able to correctly infer the target density profile).

336
337
338
339
340
341
342
343

with plentiful nominal data (like the UAV problem), training on zero-labeled nominal data also substantially boosts performance. The appendix includes further results on training time and the sensitivity of CALNF to varying K (Fig. 11), β (Fig. 12), and target dataset size N_t (Fig. 12).

344
345

4.4 USING CALNF FOR ANOMALY DETECTION

346
347
348
349
350
351
352
353
354
355
356
357

Although our main focus in this paper is modeling failure events, we can apply the posteriors learned using our method to detect previously-unseen failures. To use CALNF for anomaly detection, we train the normalizing flow and calibration label as described above, then use the ELBO $\mathcal{L}(\phi, c^*, \{x, y\})$ as the score function to classify a novel datapoint $\{x, y\}$. Table 2 shows the area under the receiver operating characteristic curve (AUROC) and area under the precision-recall curve (AUCPR) for this CALNF-based anomaly detector on the UAV and SWI problems, compared with the supervised anomaly detector proposed in (Gudovskiy et al., 2022; Kang et al., 2022; Rudolph et al., 2021) and with hand-tuned KL- and W_2 -regularized variants. We were not able to test the ATC problem in this setting due to a lack of data, and the 2D toy example is too simple to be informative, as all methods achieve near-perfect classification. Although CALNF is designed for posterior learning rather than anomaly detection, we find that it achieves more consistent results on this downstream task than existing methods, likely due to CALNF’s resistance to overfitting.

358
359
360
361
362
363
364
365
366
367
368

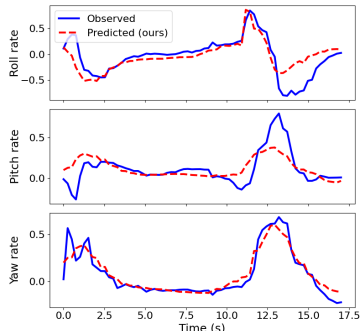


Figure 4: Single-shot UAV failure dynamics predicted by CALNF.

369
370
371
372

4.5 CALNF FOR FEW-SHOT INFERENCE ON IMAGE DATA

373
374
375
376
377

Although image modeling is not the focus of this work, for completeness we also include results applying CALNF to few-shot image generation. To use CALNF for this task, we replace the underlying normalizing flow with a conditional Glow architecture (a type of normalizing flow specialized for image modeling Kingma & Dhariwal (2018)), using the calibration label as the

Table 2: Anomaly detection performance on held-out data, reporting mean and standard deviation across four seeds.

	AUROC \uparrow		AUCPR \uparrow	
	SWI	UAV	SWI	UAV
NF-AD	0.74 \pm 0.03	0.65 \pm 0.17	0.77 \pm 0.03	0.56 \pm 0.23
NF-AD _{KL}	0.74 \pm 0.03	0.74 \pm 0.09	0.77 \pm 0.03	0.70 \pm 0.12
NF-AD _{W₂}	0.65 \pm 0.03	0.54 \pm 0.08	0.63 \pm 0.03	0.41 \pm 0.08
Ensemble	0.75 \pm 0.10	0.5 \pm 0.0	0.78 \pm 0.09	0.36 \pm 0.0
CalNF	0.79 \pm 0.02	0.70 \pm 0.03	0.83 \pm 0.03	0.66 \pm 0.04

conditioning input. We adapt the MNIST (LeCun et al., 2010) and CIFAR-10 (Krizhevsky, 2009) datasets to create a nominal dataset with all training examples from a single class and a target dataset with 64 examples from a second class. In this case, there is no underlying stochastic process and no context variables (i.e. we directly observe the images $x \sim p_\theta(x|z) = \delta(x - z)$), and the empirical ELBO (4) reduces to the average negative log likelihood of the training data. As a result, minimizing the loss (5) learns an approximation of the training image distribution.

Each method is trained on all examples from the nominal class and the limited set examples from the target class, and we report the negative log-likelihood on held-out test data, then we measure the negative log-likelihood on held-out images from the target class to test generalization beyond the limited training examples. Table 3 and Fig. 6 show the results of this experiment. We find that CALNF is able to generalize better than either a standard or ensemble model, as measured by a higher log likelihood on the held-out data

Table 3: Log-likelihood (bits/dim) on held-out images, reporting mean and standard deviation across four seeds. Higher is better.

	MNIST	CIFAR-10
Glow (vanilla)	-5.77±0.17	148.6±45.9
Glow (ensemble)	-5.77±0.17	85.91±17.5
Glow + CALNF	-5.99±0.12	23.30±12.9

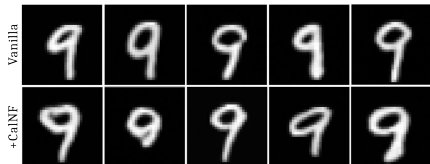


Figure 5: Samples with CALNF (bottom) are more diverse than those without (top).



Figure 6: Log-likelihood (bits/dim) on MNIST validation set; CALNF reduces overfitting to sparse examples.

5 CASE STUDY: 2022 SOUTHWEST AIRLINES SCHEDULING CRISIS

In this section, we apply CALNF to a post-mortem analysis of the 2022 Southwest Airlines scheduling crisis. Between December 21st and December 30th, 2022, a series of cascading delays and cancellations severely disrupted the Southwest network, starting in Denver and spreading across the United States. The disruption occurred in roughly two stages, as shown in Fig. 13 in the appendix. In the first stage, from 12/21 to 12/24, weather and operational difficulties caused cancellations to increase from a < 5% baseline to over 50% of scheduled flights. In the second phase between 12/25 and 12/29, Southwest flight dispatchers started preemptively canceling flights and ferrying crew between airports to reset the network, canceling up to 77% of scheduled flights before returning to near-normal operations on 12/30. Southwest ultimately canceled more than 16,000 flights, affecting more than 2 million passengers, and the airline lost substantial revenue and later paid a \$140 million penalty imposed by the US Department of Transportation (28% of its 2023 net income; (Rose, 2023)).

This incident has been the subject of extensive investigation, with a report from Southwest Airlines (Southwest Airlines, 2023), testimony before the US Senate from the Southwest Airlines Pilots Association (SWAPA; (Murray, 2023)), and press coverage (Rose, 2023; Cramer & Levenson, 2022). These sources propose a number of hypotheses on the root cause of the 2022 incident. While there is broad agreement that winter weather was a major factor, sources differ on the role of other factors; e.g. the SWAPA report emphasizes poor crew management, while press coverage emphasizes the point-to-point nature of the Southwest network.

Given this context, we have two goals for our case study. First, we are interested in identifying changes in the network state that coincided with the disruption, and how those disrupted parameters compare to the nominal state of the network. Second, we aim to produce a generative model of the disrupted network conditions for use as a tool for network design and analysis (e.g. as a simulation environment for stress-testing future scheduling and recovery policies might).

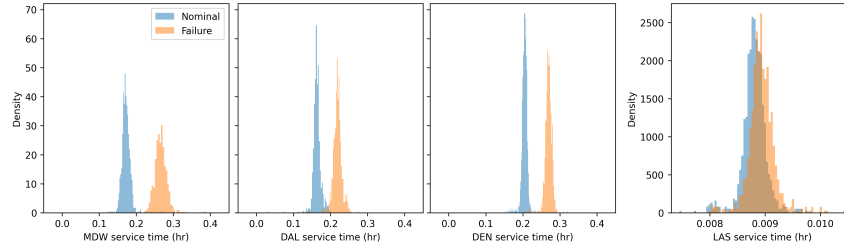


Figure 7: The posterior distribution of departure service times at DEN, MDW, DAL, and LAS. Service times increased only at airports that saw severe weather (DEN, MDW, and DAL).

5.1 IMPLEMENTATION

We focus on the first four days of the scheduling crisis, prior to the wave of manual interventions aimed at resetting the network. We conduct our analysis at two spatial resolutions, considering subnetworks of the 4 and 10 busiest airports in the Southwest network, respectively. More details on our model are included in the appendix, along with a key for relevant airport codes in Table 6.

5.2 RESULTS

Localized delays due to winter weather. Our first observation confirms a common explanation for the disruption: that localized delays at airports across the US coincided with winter weather. Fig. 7 shows CALNF’s posterior estimates of nominal and disrupted service times (a proxy for taxi, deicing, and ATC delays) at the four busiest airports. Of these four, only those that experienced severe cold temperatures (DEN, MDW, and DAL) saw an increase in average service time, while there was no significant increase at LAS, which did not have severe weather. This result agrees with official accounts that identify winter weather and a lack of deicing equipment at critical airports like DEN as contributing factors (Southwest Airlines, 2023; Cramer & Levenson, 2022). However, the more important question is how these localized service delays cascaded into the nationwide disruption.

Cascading failures due to aircraft flow interruption. Our main finding comes from modeling the movement of aircraft within the network. The number of aircraft starting the day at each airport provides an important measure of robustness, since if there are insufficient aircraft to meet demand, then departing flights must be delayed or canceled. Aircraft deficits can also cascade through the network, as down-stream airports are deprived of the aircraft needed to serve scheduled departures. Because aircraft distribution data are not publicly available, we must use our method to infer it.

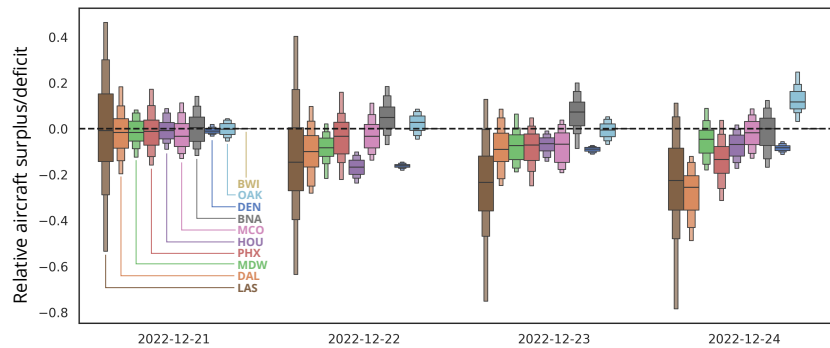


Figure 8: CALNF’s inferred posterior estimates of the distribution of Southwest aircraft at the start of the first four days of the disruption, normalized by the number of scheduled departures at each airport; positive/negative indicates more/fewer aircraft than in the nominal case, respectively. CALNF suggests that LAS, DAL, and PHX accumulated a large aircraft deficit over the course of the disruption.

Fig. 8 shows our results from using CALNF to infer the distribution of aircraft reserves in the top-10 network over each of the first four days of the disruption. CALNF finds that there was no detectable deviation from the nominal aircraft distribution on the first day of the disruption, but we infer a steadily increasing deficit at LAS, DAL, and PHX over the following three days. The fact that the aircraft deficit at these airports continued to worsen may have been a factor in Southwest’s decision to “hard reset” the network by ferrying empty planes between airports.

Beyond inferring these hidden parameters in the Southwest network, CALNF’s results also suggest a possible causal mechanism by which aircraft deficits at LAS, DAL, and PHX propagated to the rest of the network. Although the Southwest network is famously operated in a point-to-point manner, aircraft typically visit multiple airports in sequence on a given day; and disruptions at any of these intermediate destinations can lead to “missing aircraft” at downstream nodes. For example, although LAS and PHX did not experience severe weather during this period, nearly 50% of aircraft ultimately bound for LAS or PHX pass through either DEN or MDW (which did see weather-related delays). Our analysis in Fig. 8 suggests that trends in aircraft reserves at key airports like LAS, PHX, and DAL might be valuable early warning signs for detecting future disruptions.

Generative modeling Once we have learned the nominal and disruption posteriors for the Southwest network, we can use these as generative models for stress-testing proposed modifications to the Southwest network or scheduling system. In future work, we hope to explore how these generative models can be used to design more resilient schedule recovery algorithms.

6 CONCLUSION

In this paper, we propose a novel algorithm for rare-event modeling, developing a data-constrained posterior inference tool that uses a subsampling and calibration strategy to avoid overfitting to sparse data. We apply our algorithm to failure analysis and inverse problems, achieving competitive performance on a range of benchmarks with both simulated and real data. We also apply our algorithm to a real-world failure modeling problem, providing new insight into the factors behind the 2022 Southwest Airlines scheduling crisis.

Limitations & future work The primary limitation of our work is that training CALNF on randomly sampled subsets of the target dataset incurs an additional training cost (as shown in Table 9 in the appendix). Although there is no inference-time penalty, CALNF requires $K + 1$ evaluations of the joint likelihood $p(x, z; y)$ per training step (one for each of K subsamples and once for updating c^*), compared to K evaluations for the ensemble and one evaluation for the KL- and W_2 -regularized methods. **Our method also requires one additional hyperparameter than the baselines, which adds to implementation complexity, and it is more difficult to train in parallel than the ensemble model.** However, even though CALNF is slower to train, it achieves results in the low-data regime that are not possible using faster methods. For example, Fig. 3 shows how our method solves a seismic imaging problem that none of the competing baselines can solve, **and CALNF yields better, more consistent performance on downstream anomaly classification tasks.** We would also like to emphasize that there is no additional cost for our method at inference time, other than the negligible cost of passing the calibrated label c^* as an additional input to the normalizing flow.

A second limitation is that our method does not provide an estimate of the risk of failure. Estimating the probability of failure is challenging due to the size of the dataset, but we hope that future work will close this gap; e.g. providing theoretical bounds using large deviation theory (Dembo & Zeitouni, 2010). **A final limitation is that we implicitly assume that failure examples share some structure with nominal ones, and so learning a shared representation for both cases (as CALNF does) is helpful. If the failure examples are drawn from a radically different distribution than nominal data, the implicit regularization from this shared representation (discussed in Theorem 1) may not be useful.**

Broader impact This paper aims to provide tools to understand the causes of past failures and prevent future incidents. We hope that our work will help enable a more comprehensive data-driven approach to safety analysis for complex systems, including cyberphysical systems and complex infrastructural networks. There is some potential for negative impact (e.g. a bad actor attempting to infer the properties of a safety-critical system to prepare an adversarial attack), but we believe that the potential benefits for designing more robust systems outweigh these concerns.

540 **Reproducibility Statement** We include anonymized source code in a zip file in our supplementary
541 materials, including README files with instructions for installing all required dependencies and
542 scripts for recreating all experimental results reported in this paper, including all hyperparameters
543 and random seeds used.
544

545
546
547
548
549
550
551
552
553
554
555
556
557
558
559
560
561
562
563
564
565
566
567
568
569
570
571
572
573
574
575
576
577
578
579
580
581
582
583
584
585
586
587
588
589
590
591
592
593

REFERENCES

- 594
595
596 Zuko (open-source library). The Probabilists, January 2024.
- 597
598
599 Milad Abdollahzadeh, Touba Malekzadeh, Christopher T. H. Teo, Keshigeyan Chandrasegaran,
600 Guimeng Liu, and Ngai-Man Cheung. A Survey on Generative Modeling with Limited Data, Few
601 Shots, and Zero Shot, July 2023.
- 602
603
604 Muhammad Asim, Max Daniels, Oscar Leong, Ali Ahmed, and Paul Hand. Invertible generative
605 models for inverse problems: Mitigating representation error and dataset bias. In *Proceedings of
606 the 37th International Conference on Machine Learning*, pp. 399–409. PMLR, November 2020.
- 607
608
609 Jens Behrmann, Will Grathwohl, Ricky T. Q. Chen, David Duvenaud, and Joern-Henrik Jacobsen.
610 Invertible Residual Networks. In *Proceedings of the 36th International Conference on Machine
611 Learning*, pp. 573–582. PMLR, May 2019.
- 612
613
614 Eli Bingham, Jonathan P. Chen, Martin Jankowiak, Fritz Obermeyer, Neeraj Pradhan, Theofanis
615 Karaletsos, Rohit Singh, Paul Szerlip, Paul Horsfall, and Noah D. Goodman. Pyro: Deep universal
616 probabilistic programming. *The Journal of Machine Learning Research*, 20(1):973–978, January
617 2019. ISSN 1532-4435.
- 618
619
620 Leo Breiman. Bagging predictors. *Machine Learning*, 24(2):123–140, August 1996. ISSN 1573-0565.
621 doi: 10.1007/BF00058655.
- 622
623
624 Ricky T. Q. Chen, Yulia Rubanova, Jesse Bettencourt, and David K Duvenaud. Neural Ordinary
625 Differential Equations. In *Advances in Neural Information Processing Systems*, volume 31. Curran
626 Associates, Inc., 2018.
- 627
628
629 Ricky T. Q. Chen, Jens Behrmann, David K Duvenaud, and Joern-Henrik Jacobsen. Residual Flows
630 for Invertible Generative Modeling. In *Advances in Neural Information Processing Systems*,
631 volume 32. Curran Associates, Inc., 2019.
- 632
633
634 Hyunsun Choi, Eric Jang, and Alexander A. Alemi. WAIC, but Why? Generative Ensembles for
635 Robust Anomaly Detection, May 2019.
- 636
637
638 Anthony Corso, Robert Moss, Mark Koren, Ritchie Lee, and Mykel Kochenderfer. A Survey of
639 Algorithms for Black-Box Safety Validation of Cyber-Physical Systems. *Journal of Artificial
640 Intelligence Research*, 72:377–428, January 2022. ISSN 1076-9757. doi: 10.1613/jair.1.12716.
- 641
642
643 Maria Cramer and Michael Levenson. What Caused the Chaos at Southwest. *The New York Times*,
644 December 2022. ISSN 0362-4331.
- 645
646
647 Charles Dawson and Chuchu Fan. A Bayesian approach to breaking things: Efficiently predicting and
648 repairing failure modes via sampling. In *7th Annual Conference on Robot Learning*, August 2023.
- 649
650
651 Harrison Delecki, Anthony Corso, and Mykel Kochenderfer. Model-based Validation as Probabilistic
652 Inference. In *Proceedings of The 5th Annual Learning for Dynamics and Control Conference*, pp.
653 825–837. PMLR, June 2023.
- 654
655
656 Amir Dembo and Ofer Zeitouni. *Large Deviations Techniques and Applications*, volume 38 of
657 *Stochastic Modelling and Applied Probability*. Springer, Berlin, Heidelberg, 2010. ISBN 978-3-
658 642-03310-0 978-3-642-03311-7. doi: 10.1007/978-3-642-03311-7.
- 659
660
661 Chengyuan Deng, Shihang Feng, Hanchen Wang, Xitong Zhang, Peng Jin, Yinan Feng, Qili Zeng,
662 Yinpeng Chen, and Youzuo Lin. OpenFWI: Large-scale Multi-structural Benchmark Datasets for
663 Full Waveform Inversion. In *Thirty-Sixth Conference on Neural Information Processing Systems
664 Datasets and Benchmarks Track*, June 2022.
- 665
666
667 Conor Durkan, Artur Bekasov, Iain Murray, and George Papamakarios. Neural spline flows. In
668 *Proceedings of the 33rd International Conference on Neural Information Processing Systems*, pp.
669 7511–7522, Red Hook, NY, USA, December 2019. Curran Associates Inc.
- 670
671
672 Bradley Efron. Bootstrap Methods: Another Look at the Jackknife. In Samuel Kotz and Norman L.
673 Johnson (eds.), *Breakthroughs in Statistics: Methodology and Distribution*, pp. 569–593. Springer,
674 New York, NY, 1992. ISBN 978-1-4612-4380-9. doi: 10.1007/978-1-4612-4380-9_41.

- 648 Chris Finlay, Jörn-Henrik Jacobsen, Levon Nurbekyan, and Adam M Oberman. How to train
649 your neural ODE: The world of Jacobian and Kinetic regularization. In *Proceedings of the*
650 *37th International Conference on Machine Learning*, volume 119 of *ICML'20*, pp. 3154–3164.
651 JMLR.org, July 2020.
- 652 Zhengqi Gao, Dinghui Zhang, Luca Daniel, and Duane S. Boning. Rare Event Probability Learning
653 by Normalizing Flows, October 2023.
- 654 Kunal Garg, Charles Dawson, Kathleen Xu, Melkior Ornik, and Chuchu Fan. Model-Free Neural
655 Fault Detection and Isolation for Safe Control. *IEEE Control Systems Letters*, 7:3169–3174, 2023.
656 ISSN 2475-1456. doi: 10.1109/LCSYS.2023.3302768.
- 657 Wences P. Gouveia and John A. Scales. Bayesian seismic waveform inversion: Parameter estimation
658 and uncertainty analysis. *Journal of Geophysical Research: Solid Earth*, 103(B2):2759–2779,
659 1998. ISSN 2156-2202. doi: 10.1029/97JB02933.
- 660 Denis Gudovskiy, Shun Ishizaka, and Kazuki Kozuka. CFLOW-AD: Real-Time Unsupervised
661 Anomaly Detection with Localization via Conditional Normalizing Flows. In *2022 IEEE/CVF*
662 *Winter Conference on Applications of Computer Vision (WACV)*, pp. 1819–1828. IEEE Computer
663 Society, January 2022. ISBN 978-1-66540-915-5. doi: 10.1109/WACV51458.2022.00188.
- 664 Dan Hendrycks, Mantas Mazeika, and Thomas Dietterich. Deep Anomaly Detection with Outlier
665 Exposure. In *International Conference on Learning Representations*, September 2018.
- 666 Irina Higgins, Loic Matthey, Arka Pal, Christopher Burgess, Xavier Glorot, Matthew Botvinick,
667 Shakir Mohamed, and Alexander Lerchner. Beta-VAE: Learning Basic Visual Concepts with a
668 Constrained Variational Framework. In *International Conference on Learning Representations*,
669 November 2016.
- 670 Chin-Wei Huang, David Krueger, Alexandre Lacoste, and Aaron Courville. Neural Autoregressive
671 Flows. In *Proceedings of the 35th International Conference on Machine Learning*, pp. 2078–2087.
672 PMLR, July 2018.
- 673 Zhuangwei Kang, Ayan Mukhopadhyay, Aniruddha Gokhale, Shijie Wen, and Abhishek Dubey.
674 Traffic Anomaly Detection Via Conditional Normalizing Flow. In *2022 IEEE 25th International*
675 *Conference on Intelligent Transportation Systems (ITSC)*, pp. 2563–2570, Macau, China, October
676 2022. IEEE Press. doi: 10.1109/ITSC55140.2022.9922061.
- 677 Azarakhsh Keipour, Mohammadreza Mousaei, and Sebastian Scherer. ALFA: A dataset for UAV
678 fault and anomaly detection. *The International Journal of Robotics Research*, 40(2-3):515–520,
679 February 2021. ISSN 0278-3649. doi: 10.1177/0278364920966642.
- 680 Diederik P. Kingma and Max Welling. Auto-Encoding Variational Bayes. In *2nd International*
681 *Conference on Learning Representations*, December 2013.
- 682 Durk P Kingma and Prafulla Dhariwal. Glow: Generative Flow with Invertible 1x1 Convolutions. In
683 *Advances in Neural Information Processing Systems*, volume 31. Curran Associates, Inc., 2018.
- 684 Durk P Kingma, Tim Salimans, Rafal Jozefowicz, Xi Chen, Ilya Sutskever, and Max Welling. Im-
685 proved Variational Inference with Inverse Autoregressive Flow. In *Advances in Neural Information*
686 *Processing Systems*, volume 29. Curran Associates, Inc., 2016.
- 687 Chaerin Kong, Jeesoo Kim, Donghoon Han, and Nojun Kwak. Few-Shot Image Generation
688 with Mixup-Based Distance Learning. In *Computer Vision – ECCV 2022: 17th European Confer-*
689 *ence, Tel Aviv, Israel, October 23–27, 2022, Proceedings, Part XV*, pp. 563–580, Berlin, Heidelberg,
690 October 2022. Springer-Verlag. ISBN 978-3-031-19783-3. doi: 10.1007/978-3-031-19784-0_33.
- 691 Alex Krizhevsky. Learning multiple layers of features from tiny images. pp. 32–33, 2009.
- 692 Yann LeCun, Corinna Cortes, and CJ Burges. MNIST handwritten digit database. *ATT Labs [Online]*.
693 Available: <http://yann.lecun.com/exdb/mnist>, 2, 2010.

- 702 Tianci Liu, Tong Yang, Quan Zhang, and Qi Lei. Optimization for Amortized Inverse Problems. In
703 *Proceedings of the 40th International Conference on Machine Learning*, pp. 22289–22319. PMLR,
704 July 2023.
- 705 Takeru Miyato, Toshiki Kataoka, Masanori Koyama, and Yuichi Yoshida. Spectral Normalization
706 for Generative Adversarial Networks. In *International Conference on Learning Representations*,
707 February 2018.
- 708 Casey Murray. Strengthening airline operations and consumer protections, February 2023.
- 709 Naji Najari, Samuel Berlemont, Grégoire Lefebvre, Stefan Duffner, and Christophe Garcia. Robust
710 Variational Autoencoders and Normalizing Flows for Unsupervised Network Anomaly Detection.
711 In Leonard Barolli, Farookh Hussain, and Tomoya Enokido (eds.), *Advanced Information Net-*
712 *working and Applications*, pp. 281–292, Cham, 2022. Springer International Publishing. ISBN
713 978-3-030-99587-4. doi: 10.1007/978-3-030-99587-4_24.
- 714 Jeremy Nixon, Balaji Lakshminarayanan, and Dustin Tran. Why Are Bootstrapped Deep Ensembles
715 Not Better? In *“I Can’t Believe It’s Not Better!” NeurIPS 2020 Workshop*, December 2020.
- 716 Matthew O’ Kelly, Aman Sinha, Hongseok Namkoong, Russ Tedrake, and John C Duchi. Scalable
717 End-to-End Autonomous Vehicle Testing via Rare-event Simulation. In *Advances in Neural*
718 *Information Processing Systems*, volume 31. Curran Associates, Inc., 2018.
- 719 Utkarsh Ojha, Yijun Li, Jingwan Lu, Alexei A. Efros, Yong Jae Lee, Eli Shechtman, and Richard
720 Zhang. Few-shot Image Generation via Cross-domain Correspondence. In *2021 IEEE/CVF*
721 *Conference on Computer Vision and Pattern Recognition (CVPR)*, pp. 10738–10747, June 2021.
722 doi: 10.1109/CVPR46437.2021.01060.
- 723 Derek Onken, Samy Wu Fung, Xingjian Li, and Lars Ruthotto. OT-Flow: Fast and Accurate
724 Continuous Normalizing Flows via Optimal Transport. *Proceedings of the AAAI Conference on*
725 *Artificial Intelligence*, 35(10):9223–9232, May 2021. ISSN 2374-3468. doi: 10.1609/aaai.v35i10.
726 17113.
- 727 Nikolas Pyrgiotis, Kerry M. Malone, and Amedeo Odoni. Modelling delay propagation within an
728 airport network. *Transportation Research Part C: Emerging Technologies*, 27:60–75, February
729 2013. ISSN 0968-090X. doi: 10.1016/j.trc.2011.05.017.
- 730 Danilo Jimenez Rezende and Shakir Mohamed. Variational inference with normalizing flows.
731 In *Proceedings of the 32nd International Conference on International Conference on Machine*
732 *Learning - Volume 37, ICML’15*, pp. 1530–1538, Lille, France, July 2015. JMLR.org.
- 733 Alan Richardson. Deepwave. Zenodo, September 2023.
- 734 Joel Rose. Southwest will pay a \$140 million fine for its meltdown during the 2022 holidays. *NPR*,
735 December 2023.
- 736 Marco Rudolph, Bastian Wandt, and Bodo Rosenhahn. Same same but DifferNet: Semi-supervised
737 defect detection with normalizing flows. In *Winter Conference on Applications of Computer Vision*
738 *(WACV)*, January 2021.
- 739 Aman Sinha, Matthew O’ Kelly, Russ Tedrake, and John Duchi. Neural bridge sampling for evaluating
740 safety-critical autonomous systems. In *Proceedings of the 34th International Conference on Neural*
741 *Information Processing Systems, NIPS’20*, pp. 6402–6416, Red Hook, NY, USA, December 2020.
742 Curran Associates Inc. ISBN 978-1-71382-954-6.
- 743 Southwest Airlines. Final Summary and Action Plan, 2023.
- 744 A. M. Stuart. Inverse problems: A Bayesian perspective. *Acta Numerica*, 19:451–559, May 2010.
745 ISSN 1474-0508, 0962-4929. doi: 10.1017/S0962492910000061.
- 746 Esteban G. Tabak and Eric Vanden-Eijnden. Density estimation by dual ascent of the log-likelihood.
747 *Communications in Mathematical Sciences*, 8(1):217–233, March 2010. ISSN 1539-6746, 1945-
748 0796.

- 756 Toan Tran, Trung Pham, Gustavo Carneiro, Lyle Palmer, and Ian Reid. A Bayesian Data Augmentation
757 Approach for Learning Deep Models. In *Advances in Neural Information Processing Systems*,
758 volume 30. Curran Associates, Inc., 2017.
- 759 Alexandre Verine, Benjamin Negrevert, Yann Chevaleyre, and Fabrice Rossi. On the expressivity
760 of bi-Lipschitz normalizing flows. In *Proceedings of The 14th Asian Conference on Machine
761 Learning*, pp. 1054–1069. PMLR, April 2023.
- 762 Yaqing Wang, Quanming Yao, James T. Kwok, and Lionel M. Ni. Generalizing from a Few Examples:
763 A Survey on Few-shot Learning. *ACM Computing Surveys*, 53(3):63:1–63:34, June 2020. ISSN
764 0360-0300. doi: 10.1145/3386252.
- 765 Jian Zhang, Chenglong Zhao, Bingbing Ni, Minghao Xu, and Xiaokang Yang. Variational Few-Shot
766 Learning. In *Proceedings of the IEEE/CVF International Conference on Computer Vision*, pp.
767 1685–1694, 2019.
- 768 Ran Zhang, Claudia Czado, and Karin Sigloch. Bayesian Spatial Modelling for High Dimensional
769 Seismic Inverse Problems. *Journal of the Royal Statistical Society Series C: Applied Statistics*, 65
770 (2):187–213, February 2016. ISSN 0035-9254. doi: 10.1111/rssc.12118.
- 771 Chenyu Zheng, Guoqiang Wu, and Chongxuan Li. Toward Understanding Generative Data Aug-
772 mentation. In *Thirty-Seventh Conference on Neural Information Processing Systems*, November
773 2023.
- 774 Ziyuan Zhong, Davis Rempe, Danfei Xu, Yuxiao Chen, Sushant Veer, Tong Che, Baishakhi Ray, and
775 Marco Pavone. Guided Conditional Diffusion for Controllable Traffic Simulation. In *2023 IEEE
776 International Conference on Robotics and Automation (ICRA)*, pp. 3560–3566, May 2023. doi:
777 10.1109/ICRA48891.2023.10161463.

783 A LIPSCHITZ CONSTANTS FOR CONDITIONAL NORMALIZING FLOWS

784 In this section, we provide the Lipschitz constants for various conditional normalizing flow architec-
785 tures; i.e. L such that $|f(z, c_1) - f(z, c_2)| \leq L \|c_1 - c_2\|$ for all z, c_1, c_2 .

786 *Remark 1.* The conditional inverse autoregressive flow (IAF; (Kingma et al., 2016)) has Lipschitz
787 constant $L \leq \prod_i \prod_t (L_{s_t} + L_{m_t})$, where the outer product is over autoregressive blocks and the
788 inner product is over steps within each autoregressive block. L_{s_t} and L_{m_t} are the Lipschitz constants
789 of the neural networks yielding the m_t and s_t values for each autoregressive step (these can be
790 easily bounded for most neural networks; e.g. by the product of the L_2 matrix norms of the weight
791 matrices; (Miyato et al., 2018)).

792 *Remark 2.* A neural spline flow (Durkan et al., 2019) has Lipschitz constant $L \leq 2\bar{s}$, where \bar{s} is an
793 upper bound on the slope $s = (y_{k+1} - y)/(x_{k+1} - x_k)$ between adjacent knot points of the spline
794 (this can be constrained by construction by ensuring a minimum spline bin width).

795 *Remark 3.* Continuous normalizing flows (Chen et al., 2018) have Lipschitz constant $L \leq e^{L_g \Delta t}$
796 where Δt is the duration of integration and L_g is the Lipschitz constant of the neural network defining
797 the vector field of the flow.

798 *Remark 4* (from (Verine et al., 2023)). Normalizing flows based on invertible residual networks, such
799 as i-ResNet (Behrmann et al., 2019) and Residual Flow (Chen et al., 2019), have Lipschitz constant
800 $L \leq (1 + L_g)^m$, where m is the number of residual blocks and $L_g < 1$ is the Lipschitz constant of
801 the residual block $g(x)$.

802 *Remark 5* (from (Verine et al., 2023)). Normalizing flows based on Glow (Kingma & Dhariwal,
803 2018) have Lipschitz constant $L \leq \prod \|W_i\|_2$, where the product is over the weight matrices W_i of
804 the convolution blocks.

806 B PROOF OF LEMMA 1

807 *Proof.* The optimal maximum likelihood estimator is a mixture of delta functions $q^*(z) =$
808 $\sum_{z^{(i)} \in \mathcal{D}} \delta(z - z^{(i)})/N$. Since we assume that the data points are well-separated, the optimal
809

810 L -Lipschitz maximum likelihood estimator replaces the scaled delta $\delta(z)/N$ with the L -Lipschitz
 811 function $\hat{\delta}(z)$ that a) is non-negative, b) integrates to $1/N$, and c) maximizes the value $\hat{\delta}(0)$. Con-
 812 straint (c) will be active (otherwise we recover the scaled delta function), so we know that $\hat{\delta}$ will have
 813 the form $\max(0, a - L\|z\|)$. Normalizing to $1/N$ yields
 814

$$815 \hat{\delta}(z) = \max(0, a - L\|z\|) \quad (6)$$

$$816 a = \left(\frac{(d+1)L^d \Gamma(\frac{d}{2} + 1)}{\pi^{d/2} N} \right)^{1/(d+1)} \quad (7)$$

820 Substituting one data point for another (subject to the assumption on data sparsity) changes the
 821 optimal estimator by swapping the corresponding mixture component; i.e. exchanging $\hat{\delta}(z - z^{(2)})$
 822 for $\hat{\delta}(z - z^{(1)})$. The W_2 distance between the resulting mixtures is the same as the W_2 distance
 823 between the changed components. Each component has probability mass $1/N$ and they are distance
 824 $\|z^{(1)} - z^{(2)}\|$ apart, completing the proof. \square
 825

826 C PROOF OF LEMMA 2

827 *Proof.* Let \mathcal{D}_i be a random dataset created by sampling \mathcal{D} N times with replacement. In the proof
 828 of Lemma 1, we show that the optimal L -Lipschitz maximum likelihood estimator given \mathcal{D}_i is
 829 $\sum_{z \in \mathcal{D}_i} \hat{\delta}(z - z^{(i)})$. This gives ensemble model
 830

$$831 q_{\text{ensemble}}(z) = \sum_{i=1}^K \left[\sum_{z \in \mathcal{D}_i} \hat{\delta}(z - z^{(i)}) \right] / K \quad (8)$$

832 Since each \mathcal{D}_i is sampled independently with replacement, we can combine the nested sums
 833

$$834 q_{\text{ensemble}}(z) = \sum_{z^{(i)} \in \mathcal{D}_{NK}} \hat{\delta}(z - z^{(i)}) / K \quad (9)$$

835 where \mathcal{D}_{NK} is a single dataset of NK points sampled with replacement from \mathcal{D} . As $K \rightarrow \infty$, the
 836 empirical distribution of \mathcal{D}_{NK} approaches that of \mathcal{D} , so this sum reduces almost surely to:
 837

$$838 \lim_{K \rightarrow \infty} q_{\text{ensemble}}(z) \stackrel{a.s.}{=} \sum_{z^{(i)} \in \mathcal{D}} \hat{\delta}(z - z^{(i)}) \quad (10)$$

839 \square
 840

841 D PROOF OF THEOREM 1

842 *Proof.* The W_2 metric is defined as an infimum over couplings γ , so in order to provide an upper
 843 bound it suffices to propose a coupling between the nominal and target posteriors, $q_\phi(z, \mathbf{0}_K)$ and
 844 $q_\phi(z, c^*)$. Recall that the normalizing flow q_ϕ has base distribution q_0 and flow map f_ϕ , where $f_\phi(z, c)$
 845 is assumed to be L -Lipschitz in the second argument. Consider the joint distribution $\gamma(z_1, z_2)$ defined
 846 by $z_0 \sim q_0(z)$, $z_1 = f_\phi(z_0, \mathbf{0}_K)$, and $z_2 = f_\phi(z_0, c^*)$. By construction, the marginals of γ in each
 847 argument are $q_\phi(z, \mathbf{0}_K)$ and $q_\phi(z, c^*)$, respectively, and so γ is a valid coupling.
 848

849 This provides the bound
 850

$$851 W_2(q_\phi(\cdot, \mathbf{0}_K), q_\phi(\cdot, c^*)) \leq \left[\mathbb{E}_{z_1, z_2 \sim \gamma} \|z_1 - z_2\|^2 \right]^{1/2}$$

$$852 \leq [L^2 \|c^* - \mathbf{0}_K\|^2]^{1/2}$$

$$853 \leq L \|c^*\|$$

854 \square
 855

E DETAILS ON BENCHMARK PROBLEMS

This section provides additional details for the three types of inverse problem studied in our paper. All problems are implemented using the Pyro probabilistic programming framework (Bingham et al., 2019).

E.1 SEISMIC WAVEFORM INVERSION

An illustration of the SWI problem is given in Fig. 9. We implement the SWI problem using the Deepwave library (Richardson, 2023). We use latent parameters $z \in \mathbb{R}^{n_x \times n_y}$ representing the subsurface density profile (with spatial resolution $n_x = 10$ and $n_y = 10$), context $y \in \mathbb{R}^{n_T}$ representing the source signal, and observations $x \in \mathbb{R}^{n_s \times n_r \times n_T}$ representing the signal measured at each receiver, where $n_s = 1, n_r = 9, n_T = 100$ are the number of sources, receivers, and timesteps, respectively. Before solving the elastic wave PDE, the density profile is upsampled to 100×30 . The observations are corrupted with additive isotropic Gaussian noise. The parameters of this problem are summarized in Table 4.

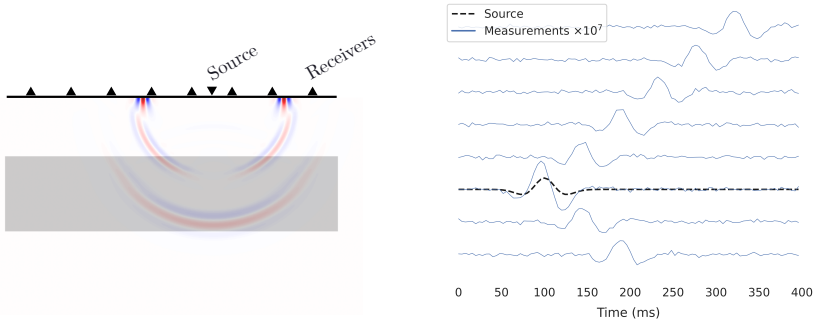


Figure 9: (Left) An illustration of the SWI problem and (right) the receiver measurements (blue) given a source signal (black).

Table 4: Summary of parameters for the SWI problem.

	Dimension
Latent parameters z	
Density profile (10×10)	100
Context y	
—	
Observation x	
Seismic waveform (100 timesteps at 9 receivers)	900

E.2 UAV CONTROL

We model the nonlinear attitude dynamics of the UAV as a combination of an unknown linear mapping from the current and desired states to angular rates, then a nonlinear mapping from angular rates to updated UAV orientation. The state $q = [\phi, \theta, \psi]$ includes the roll, pitch, and yaw angles of the UAV, and \hat{q} denotes the commanded orientation. We model the angular rates of the UAV as

$$\omega = \begin{bmatrix} p \\ q \\ r \end{bmatrix} = Aq + K(\hat{q} - q) + d + \eta \tag{11}$$

where A , K , and d are unknown feedforward, feedback, and bias dynamics, and η is Gaussian process noise. The state derivative is related to ω by

$$\frac{d}{dt}q = J^{-1}(q)\omega \quad (12)$$

$$J^{-1}(q) = \begin{bmatrix} 1 & \tan(\theta) \sin(\phi) & \tan(\phi) \cos(\theta) \\ 0 & \cos(\phi) & -\sin(\phi) \\ 0 & \sin(\phi)/\cos(\theta) & \cos(\phi)/\cos(\theta) \end{bmatrix} \quad (13)$$

We apply a first-order time discretization to yield the one-step stochastic dynamics

$$q_{t+1} = q_t + \delta_t J^{-1}(q) (Aq + K(\hat{q} - q) + d + \eta)$$

and observed states are additionally corrupted by Gaussian noise. A summary of the parameters for this problem are given in Table 5.

An example trajectory, including both nominal and anomalous segments, for the UAV dataset are shown in Fig. 10. In this case, the anomaly is relatively easy to detect; the challenge is understanding how the aircraft’s flight dynamics change during the failure so that a recovery controller can be designed to handle this case.

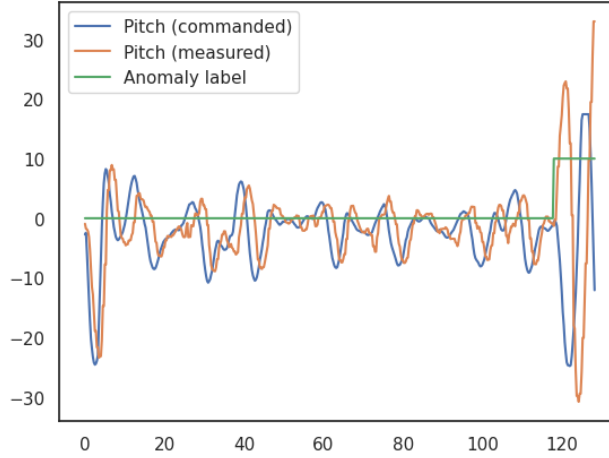


Figure 10: Example trajectory that includes an elevator failure, including both nominal and anomalous segments.

Table 5: Summary of parameters for the UAV problem.

	Dimension
Latent parameters z	
Feedforward matrix A (3×3)	9
Feedback matrix K (3×3)	9
Bias term d	3
Context y	
Current state	3
Desired orientation	3
Observation x	
Next state	3

E.3 AIR TRAFFIC NETWORK

The input to our air traffic model is a list of scheduled flights, each specifying an origin and destination airport and a scheduled departure and arrival time. The latent state z includes the mean travel time

972 between each origin/destination pair, the mean service time at each airport (which affects both arriving
 973 and departing aircraft and models taxi, deicing, and ATC delays), the mean turnaround time at each
 974 airport (the minimum time that must elapse before an arriving aircraft may depart), the baseline
 975 cancellation rate at each airport, and the initial number of aircraft at each airport. A summary of these
 976 parameters are given in Table 7. So that the benchmarks in Section 4 can be run in a reasonable time,
 977 we restrict the ATC problem used for benchmarking to the four busiest airports and do not model
 978 cancellations, but we use the ten busiest airports and do include cancellations in our case study in
 979 Section 5.

980 The model steps through the scheduled flights in 15 minute increments. In each increment, it checks
 981 for the flights that are scheduled to depart from each airport. Each of these flights receives a certain
 982 probability of cancellation given by

$$983 \quad P(\text{canceled}) = 1 - (1 - p_c)\sigma\left(10\frac{\# \text{ available aircraft}}{\# \text{ departing flights in this block}}\right) \quad (14)$$

984 where p_c is the baseline cancellation rate for the origin airport and σ is the sigmoid function, so the
 985 probability of cancellation is p_c when there are more available aircraft than scheduled departures and
 986 approaches 1 as the number of available aircraft decreases. Cancellations are sampled from a relaxed
 987 Bernoulli distribution with this cancellation probability and a straight-through gradient estimator. If a
 988 flight is canceled, it is marked as such and the observation for that flight will just be `canceled` and
 989 will not include actual departure and arrival times. If the flight is not canceled, then it is moved to the
 990 runway queue if there are enough aircraft available; otherwise, it is delayed until the next time block.

991 Both departing and arriving flights are served using a single M/M/1 queue for each airport, with
 992 service times drawn from an exponential distribution with the mean specified according to each
 993 airport’s mean service time. Once airborne, departing flights are assigned a random flight time from a
 994 Gaussian with mean given by the mean travel time for each route and fixed variance. Once this travel
 995 time has elapsed, they enter the runway queue at the destination airport. Once an aircraft has landed,
 996 it does not become available to serve new flights until the minimum turnaround time has elapsed
 997 (which is sampled from a Gaussian with mean given by the mean turnaround time for each airport).
 998 Observations for non-canceled flights include the simulated arrival and departure times, plus some
 999 fixed-variance Gaussian noise.
 1000

1001 Table 6: International Air Transport Association (IATA) codes and full names of the ten busiest
 1002 airports in the Southwest network.
 1003

1004	DEN	Denver International Airport
1005	DAL	Dallas Love Field Airport
1006	MDW	Chicago Midway International Airport
1007	PHX	Phoenix Sky Harbor International Airport
1008	HOU	William P. Hobby Airport
1009	LAS	McCarran International Airport
1010	MCO	Orlando International Airport
1011	BNA	Nashville International Airport
1012	BWI	Baltimore/Washington International Thurgood Marshall Airport
1013	OAK	Oakland International Airport

1014 E.4 TOY 2D PROBLEM

1015 The data for the 2D toy problem is generated by uniformly sampling nominal data:

$$1016 \quad \begin{aligned} 1017 \quad \theta &\sim \mathcal{U}(0, \pi) \\ 1018 \quad x &\sim \mathcal{N}(\cos \theta - 0.5, 0.1) \\ 1019 \quad y &\sim \mathcal{N}(\sin \theta - 0.25, 0.1) \end{aligned}$$

1020 and anomaly data

$$1021 \quad \begin{aligned} 1022 \quad \theta &\sim \mathcal{U}(\pi, 2\pi) \\ 1023 \quad x &\sim \mathcal{N}(\cos \theta + 0.5, 0.1) \\ 1024 \quad y &\sim \mathcal{N}(\sin \theta + 0.75, 0.1) \end{aligned}$$

Table 7: Summary of parameters for the ATC problem. n_{airport} indicates the number of airports in the model. n_{flights} indicates the total number of scheduled flights. \dagger indicates parameters that are only included in the case study.

	Dimension	Top-4 (Section 4)	Top-10 (Section 5)
Latent parameters z			
Log. of turnaround time at each airport (mean minimum delay between arrival and departure)	n_{airport}	4	10
Log. of service time at each airport (mean delay between pushback and takeoff)	n_{airport}	4	10
Log. of mean travel times between each airport	n_{airport}^2	16	100
Log. of initial aircraft reserves at each airport	$n_{\text{airport}}^\dagger$	–	10
Log. of baseline cancellation probability at each airport	$n_{\text{airport}}^\dagger$	–	10
Context y			
Scheduled arrival time of each flight	n_{flights}	44–102	405–497
Scheduled departure time of each flight	n_{flights}	44–102	405–497
Observation x			
Actual arrival time of each flight	n_{flights}	44–102	405–497
Actual departure time of each flight	n_{flights}	44–102	405–497
Whether each flight was cancelled	n_{flights}	44–102	405–497

Since this problem is meant as an easy-to-visualize test for whether a method can learn a posterior distribution with a complex shape, we set $[x, y]$ as the latent parameters and assume they are observed directly (with the addition of Gaussian noise), rather than treating θ as the latent parameter (which would lead to a very easy-to-fit posterior).

F IMPLEMENTATION DETAILS

We implement CALNF using neural spline flows (NSF) as the underlying normalizing flow (Durkan et al., 2019). We note that CALNF is agnostic to the underlying flow architecture; we also tried using masked autoregressive flows (Huang et al., 2018), which trained faster but had slightly worse performance, and continuous normalizing flows (Chen et al., 2018), which trained much more slowly.

We implement the KL regularization baseline using neural spline flows with a KL regularization penalty between the learned anomaly and nominal posteriors. We implement an RNODE-derived method that includes only the W_2 regularization term, not the Froebenius norm regularization term (which is used only to speed training and inference, not to regularize the learned posterior; (Finlay et al., 2020)).

We extend our method to anomaly detection by defining a score function as the ELBO of a given observation, approximated using 10 samples from the learned posterior.

All methods were implemented in Pytorch using the Zuko library for normalizing flows (Zuk, 2024). The neural spline flows used 3 stacked transforms, and all flows used two hidden layers of 64 units each with ReLU activation (except for the continuous flows on the 2D problem, which use two hidden layers of 128 units each). All flows were trained using the Adam optimizer with the learning rate 10^{-3} (except on the UAV problem, which used a learning rate of 10^{-2}) and gradient clipping. CALNF used $K = 5$ on all problems. All methods were trained on either a single NVIDIA GeForce RTX 2080 Ti GPU or a `g4dn.xlarge` AWS instance, with 200, 500, 500, and 150 epochs for the 2D, SWI, UAV, and ATC problems, respectively. The image generation examples were trained for 1000 epochs (MNIST) and 500 epochs (CIFAR-10). Non-image benchmarks all take less than 2 hours to train, and image benchmarks take approximately 20 hours to train. We estimate cloud compute costs for this entire project (including preliminary experiments) at less than 200 USD.

Code examples, including scripts for reproducing the results in Tables 1 and 8 and notebooks containing our data analysis for Section 5, are included in the attached supplementary material.

G FURTHER EMPIRICAL RESULTS

Table 8: ELBO (nats/dim) on held-out target data for ablations of CALNF. The first is our proposed method, the second fixes c , the third excludes the nominal data during training, and the fourth does not subsample the target data. † scaled by $\times 10^{-3}$

	2D	SWI †	UAV	ATC †
CALNF	-0.90 \pm 0.1	46.3 \pm 0.2	6.95 \pm 1.2	-2.01 \pm 0.1
w/o c^*	-0.96 \pm 0.2	46.2 \pm 0.4	7.86 \pm 1.0	-2.02 \pm 0.1
w/o \mathcal{D}_0	-1.12 \pm 0.2	46.1 \pm 0.4	-9.22 \pm 10	-2.03 \pm 0.2
w/o \mathcal{D}_t^i	-1.03 \pm 0.2	43.9 \pm 2.8	-3.65 \pm 11	-2.05 \pm 0.1

Fig. 11 shows the sensitivity of our method to different values of K on the SWI benchmark. We find that there is a slight trend towards better performance as K increases, and that including the calibration step (rather than using a fixed c^*) improves performance at all levels of K .

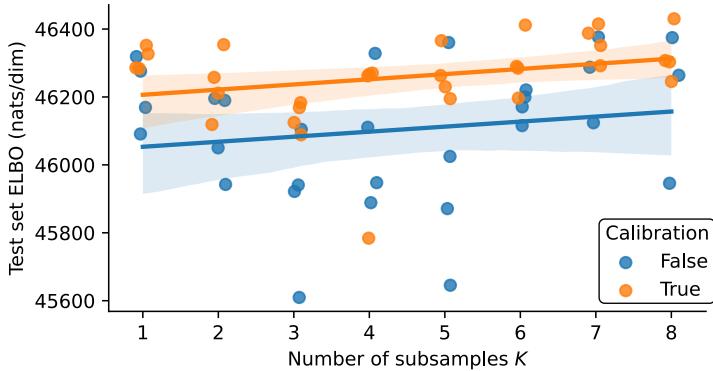


Figure 11: The ELBO on a held-out test set for the anomaly posterior learned using CALNF on the SWI example using a varying number of subsamples.

Table 9 includes the training times for our method and each baseline. We can also compare these methods theoretically in terms of the number of evaluations of the joint likelihood $p(x, z; y)$ in Eq. (4). The KL- and W_2 -regularized methods require one evaluation per training step, the ensemble method requires K evaluations, and our method requires $K + 1$. The inference times are identical except for the W_2 -regularized method, which is slower due to its use of neural ODEs for the flow map).

Fig. 12 show the performance of CALNF on the 2D benchmark as the number of target data points is decreased. When the size of the target dataset is at least 10% the size of the nominal dataset, CALNF’s test-set ELBO saturates at a high value. Between 2% and 5%, CALNF’s performance

Table 9: Training time (minutes) on benchmark problems. Mean and standard deviation reported over four random seeds.

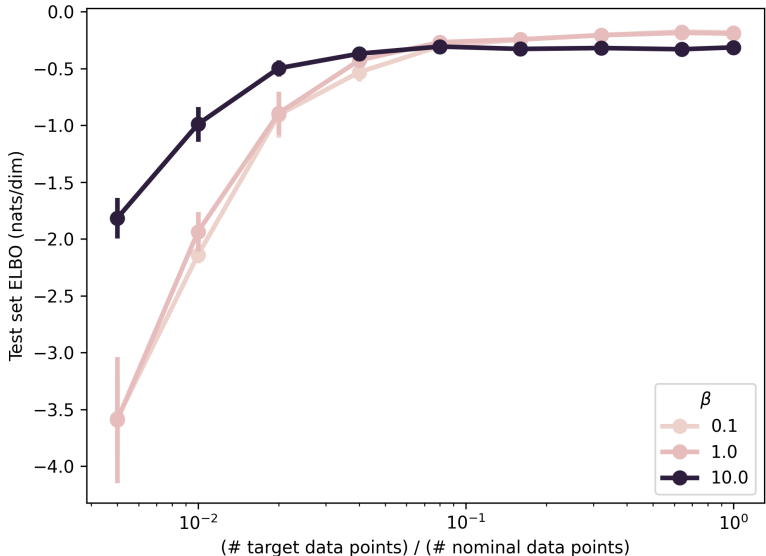
	2D	SWI	UAV	ATC
KL-regularized ($\beta = 0.01$)	1.25 \pm 0.30	6.48 \pm 0.14	31.17 \pm 0.37	84.29 \pm 1.32
KL-regularized ($\beta = 0.1$)	1.26 \pm 0.13	6.53 \pm 0.18	31.20 \pm 0.34	84.39 \pm 0.88
KL-regularized ($\beta = 1.0$)	1.34 \pm 0.05	6.58 \pm 0.18	31.24 \pm 0.16	84.09 \pm 0.78
W_2 -regularized ($\beta = 0.01$)	8.70 \pm 0.43	8.50 \pm 0.25	23.93 \pm 0.87	94.64 \pm 1.36
W_2 -regularized ($\beta = 0.1$)	8.59 \pm 0.49	8.27 \pm 0.42	23.54 \pm 0.62	93.98 \pm 1.58
W_2 -regularized ($\beta = 1.0$)	8.40 \pm 0.50	8.40 \pm 0.38	23.96 \pm 0.54	93.99 \pm 1.22
Ensemble	1.58 \pm 0.26	14.25 \pm 0.30	76.24 \pm 0.28	147.91 \pm 6.81
CalNF (ours)	2.35 \pm 0.37	19.74 \pm 0.28	77.74 \pm 0.71	174.49 \pm 6.87

1134 Table 10: ELBO (nats/dim) on held-out anomaly data of the ensemble baseline trained without
 1135 nominal data. The second and third rows are replicated from Table 1 for ease of comparison.
 1136

	2D (nats/dim) \uparrow	SWI (nats/dim) \uparrow	UAV (nats/dim) \uparrow	ATC (nats/dim) \uparrow
Ensemble (w/o nominal data)	-1.33 ± 0.23	45.93 ± 0.61	-5.81 ± 3.41	-2.07 ± 0.11
Ensemble (w/ nominal data)	-0.84 ± 0.14	46.1 ± 0.42	6.65 ± 0.98	-2.23 ± 0.06
CalNF (ours)	-0.90 ± 0.10	46.4 ± 0.26	7.55 ± 0.60	-2.11 ± 0.13

1143
 1144 begins to deteriorate, and below 2% performance drops off sharply. Higher values of β improve
 1145 performance in extremely data-sparse cases, but decrease performance when many target data points
 1146 are available. This example uses 1000 nominal data points; the results in our main paper use $\beta = 1.0$
 1147 (constant across all experiments) and a target dataset 2% of the size of the nominal dataset for this
 1148 problem.
 1149

1150 From the results in Fig. 12, we see that larger values of β perform better when the failure dataset
 1151 is very small, but smaller values of β perform better when the failure dataset is large. These results
 1152 suggest that when plenty of information is available (in the form of a large training dataset), it
 1153 is beneficial to encourage diversity among the candidate posteriors through a small regularization
 1154 strength β ; however, when information is limited, we can achieve better performance by encouraging
 1155 similarity between candidate posteriors to reduce overfitting.
 1156



1157
 1158 Figure 12: Performance of CALNF under extreme data scarcity on the 2D benchmark, with varying
 1159 self-regularization strengths β .
 1160
 1161
 1162
 1163
 1164
 1165
 1166
 1167
 1168
 1169
 1170
 1171
 1172

1173 Table 10 includes additional results comparing the performance of the ensemble method both with
 1174 and without simultaneous training on the nominal dataset, with the performance of our method from
 1175 Table 1 included for ease of reference.
 1176
 1177

1178 H ADDITIONAL RESULTS ON SOUTHWEST AIRLINES CASE STUDY
 1179
 1180
 1181

1182 A timeline of the 2022 Southwest Airlines scheduling crisis is shown in Fig. 13.
 1183
 1184
 1185
 1186
 1187

1188
1189
1190
1191
1192
1193
1194
1195
1196
1197
1198
1199
1200
1201
1202
1203
1204
1205
1206
1207
1208
1209
1210
1211
1212
1213
1214
1215
1216
1217
1218
1219
1220
1221
1222
1223
1224
1225
1226
1227
1228
1229
1230
1231
1232
1233
1234
1235
1236
1237
1238
1239
1240
1241

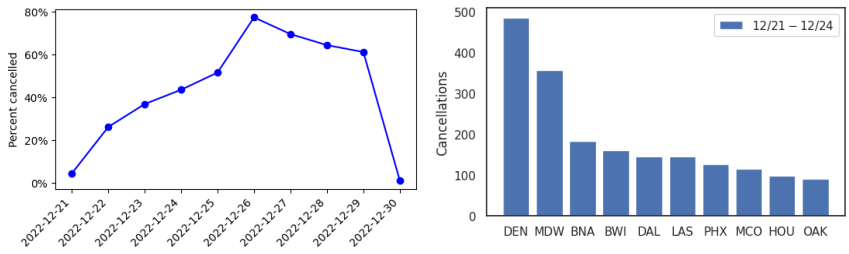


Figure 13: (Left) Timeline of cancellations during the 2022 Southwest Airlines scheduling crisis. (Right) Cancellations at the 10 busiest airports during the first four days of the disruption.